In-situ reduction of Ag nanoparticles on oxygenated mesoporous carbon fabric: Exceptional catalyst for nitroaromatics reduction

Tuo Ji [a], Long Chen [a], Liwen Mu [a], Ruixia Yuan [a], Michael Knoblauch [a], Forrest Sheng Bao [b], Jiahua Zhu [a],*

[a] *Intelligent Composites Laboratory, Department of Chemical and Biomolecular Engineering, The University of Akron, Akron, OH 44325 USA*
[b] *Department of Electrical and Computer Engineering, The University of Akron, Akron, OH 44325 USA*

ARTICLE INFO

ABSTRACT

A chemical-free method is developed to convert cotton fabric into reactive mesoporous carbon *via* optimized carbonization and oxidation processes. The processed carbon serves as both catalyst support and reactant which controls the nucleation/growth of Ag nanoparticles. The particle size is successfully controlled below 5 nm with mono-dispersion on carbon support. Various characterization techniques including scanning/transmission electron microscopies, N_2 adsorption–desorption, X-ray diffraction, X-ray photoelectron spectrum are used to study the evolution of carbon support microstructure and surface composition during thermal oxidation as well as the *in-situ* reaction between carbon support and Ag precursor during hybridization. These Ag/carbon catalysts, with well-controlled Ag nanoparticle size and excellent dispersion, out-perform other existing catalysts reported from literature in terms of activity and stability. The unique property of these catalysts promises potential applications in other chemical reactions besides the demonstrated capability in nitroaromatics reduction. Moreover, this green technology of processing biomass into effective catalyst support provides a great platform to design metal/carbon hybrid catalysts from wider biomass resources and target to broader catalytic reactions.

© 2015 Elsevier B.V. All rights reserved.

1. Introduction

Carbon supported functional nanocomposites are attracting increasing interests due to their unique physicochemical properties and versatile applications in the fields of catalysis [1–3], energy storage/conversion [4,5], sensing [6,7], environmental remediation [8,9] and *etc*. The synergistic integration of functional nanostructures and carbon support enables a rational design of desired physicochemical properties in hybrid materials, including porosity, thermal stability, surface functionality, chemical reactivity and *etc*. Among the versatile nanocomposites, metal/carbon hybrid has demonstrated highly activity and efficiency in various catalytic reactions. The major research thrust is to control metal nanoparticle size, dispersion quality and stability on carbon support and hence maximize the efficiency of the metal surface atoms for targeted reactions.

The metal nanoparticle structure and dispersion largely depend on the property of carbon support, including the surface texture (surface area and pore structure) and surface chemistry (type and density of surface functional groups). Higher surface area provides larger space to accommodate nanoparticles and artificially introduced functional groups are able to facilitate the *in-situ* nanoparticle nucleation and growth on the surface for dispersion purpose [10,11]. Without surface property control, large metal nanoparticle size with broad size distribution has been observed in previous reports [12–14]. Conventionally, regulating surface texture and manipulating surface chemistry are processed in separate steps [15–18]. For example, mesoporous carbon was firstly synthesized by template method and the carbon surface was modified by a subsequent chemical oxidation process [19,20]. Although the hybrid material after growing nanocatalysts showed good catalytic property, the complicated manufacturing procedure and heavily involved chemicals in multiple steps prevent these materials from practical applications considering the economic and environmental facts.

Sustainable chemistry advocates to promote the value of renewable resources and produce high-quality products *via* an environmentally friend approach [21]. Utilizing biomass as carbon source to synthesize carbon-based catalysts seems a promising approach. Some researchers have successfully developed metal

(Au, Pt, Pd or Ag)/carbon hybrid catalysts by using biomass (wood, pollen grains, coconut shell and cellulose) as carbon precursor [22–25]. Among the studied metal catalysts, the development of silver based catalyst is highly preferred due to its lower cost than other noble metals. However, the sacrifice of catalytic activity seems unavoidable. In fact, the particle size and dispersion of active metals play critical roles in catalytic reactions [26–28]. Therefore, it is proposed that the tradeoff of catalyst activity loss by using low cost Ag material could be eliminated if the Ag size and dispersion can be well controlled through engineering carbon surface texture and chemistry.

In-situ reduction of metal precursor into metallic nanoparticles on catalyst supports can be achieved *via* creating reactive surface functional groups [19,24,29]. It will be ideal to create a carbon platform directly from biomass with large surface area and reactive surface groups. The large surface area will help to accommodate the highest possible nanoparticle loading and the reactive surface groups will facilitate the *in-situ* nucleation and thus prevent nanoparticle migration to form larger aggregates. Recently, our group reported a unique structured hybrid catalyst with monodispersed Ag nanoparticles on hierarchical macrotube/mesopore carbon and this material shows excellent catalytic activity in nitrophenol reduction [24]. In this study, the catalyst activity is restricted by the Ag nanoparticle size, which remains a challenge to further decrease particle size down to <10.0 nm. Therefore, it will be interesting to explore how much the catalytic activity can be further enhanced by decreasing Ag particle size to less than 5.0 nm.

Herein, we present a chemical-free approach to convert cotton fabric into carbon support with large surface area and reactive surface functional groups *via* consecutive carbonization and oxidation processes. Ag precursor was *in-situ* reduced by the functional groups on carbon surface and formed <5.0 nm Ag nanoparticles with uniform distribution. Neither additional reducing agent nor stabilizer was added to control the particle size and dispersion. The structural and compositional evolution during the carbonization and oxidation processes was characterized and the reaction mechanism between Ag precursor and reactive carbon support was investigated. Nitroaromatics reduction is chosen as a model reaction to evaluate the Ag/carbon catalyst activity. The catalyst stability was also studied in cycling tests.

2. Experimental

2.1. Materials

Silver nitrate (AgNO$_3$, ≥99%), 4-nitrophenol (4-NP, ≥99%), 2-nitrophenol (2-NP, ≥99%), 4-nitroaniline (4-NA, ≥99%) and 2-nitroaniline (2-NA, 98%) were purchased from Sigma–Aldrich. Sodium borohydride (NaBH$_4$, ≥99%) was purchased from Fluka Chemical Corp. Ammonium hydroxide (NH$_4$OH, 28–30%) was purchased from BDH Chemistry. Cotton fabric was cut from a commercially available T-Shirt (100% cotton). All the chemicals were used as received without further purification. Deionized water (Millipore) was used throughout the experiment.

2.2. Synthesis of porous carbon support

Porous carbon support was prepared from cotton fabric by two consecutive steps: carbonization and oxidation. Specifically, cotton fabric was firstly carbonized in nitrogen atmosphere at 800 °C for 2 h with a heating rate of 5 °C min^{-1} and the product was named C-cotton. In order to introduce surface functional groups and create mesopore structure, the C-cotton was further oxidized in air at different temperatures (250, 350 and 370 °C) for 3 h with a heat-

ing rate of 5 °C min^{-1}. The samples oxidized at 250, 350 and 370 °C were denoted as C-250, C-350 and C-370, respectively.

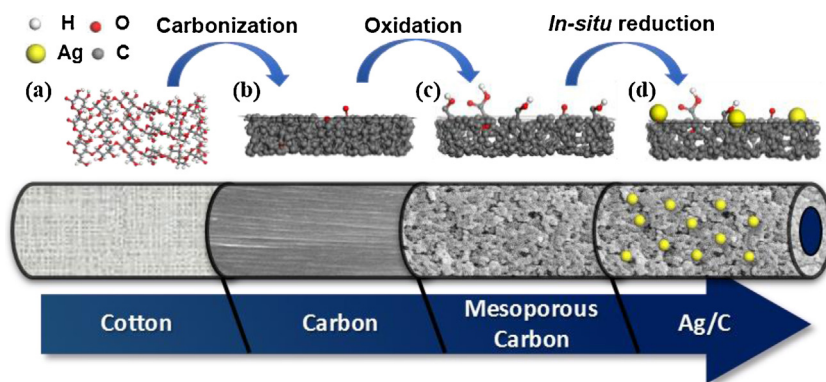### 2.3. Synthesis of Ag/carbon (Ag/C) nanocomposites

Fresh Ag(NH$_3$)$_2$NO$_3$ solution (5 mM) was prepared by dropwise addition of 10 wt% aqueous ammonia into 20.0 mL AgNO$_3$ aqueous solution until the solution turns clear. Then, 0.4 g carbon support was added into 20.0 mL ethanol:Ag(NH$_3$)$_2$NO$_3$ mixture solution (1:4, v/v). The mixture was then stirred at 40 °C for 30 min. The product was filtered, rinsed with 500 mL deionized water and dried at 70 °C for 12 h to obtain the Ag/C nanocomposite. C-cotton and three oxidized carbons were used as catalyst support and the products were named Ag/C-cotton, Ag/C-250, Ag/C-350 and Ag/C-370, respectively. To study the Ag loading effect, C-370 was selected as catalyst support to react with Ag(NH$_3$)$_2$NO$_3$ of different concentrations (5, 8 and 20 mM) and the products were named as Ag-1/C-370, Ag-2/C-370 and Ag-3/C-370, respectively.

2.4. Characterization

The sample morphology was characterized by scanning electron microscopy (SEM, JEOL-7401) with a sputter-coated gold layer on sample surface. Ag nanoparticle size and morphology was further characterized by transmission electron microscopy (FEI Scanning TEM) and High Resolution TEM (HRTEM, FEI Tecnai G2 F20 ST TEM/STEM & EDAX energy dispersive X-ray spectrometer). Samples for TEM characterization were prepared by drying a drop of sample powder ethanol suspension on carbon-coated copper TEM grids. The powder X-ray diffraction analysis was carried out with a Bruker AXS D8 Discover diffractometer with GADDS (General Area Detector Diffraction System) operating with a Cu-K α radiation source filtered with a graphite monochromator (λ = 1.541 Å). X-ray photoelectron spectroscopy (XPS) was accomplished using a PHI VersaProbe II Scanning XPS Microprobe with Al-K α line excitation source. Thermogravimetric analysis–mass spectrometry (TGA–MS) was used to analyze the surface oxygen-containing groups up to 900 °C with heating rate of 10 °C/min under argon atmosphere. Water contact angle images of carbon supports were collected by Rame-hart image system. Brunaure–Emmet–Teller (BET) surface area analysis of samples was performed using a TriStar II 3020 surface analyzer (Micromeritics Instrument Corp., USA) by N$_2$ adsorption–desorption isotherms at 77 K. The pore size distribution was calculated by the Barret Joyner and Halenda (BJH) method from adsorption branch. The Ag nanoparticle loading was determined by thermogravimetric analysis (TGA, TA instrument Q500) in air atmosphere from 20 to 700 °C with a heating rate of 10 °C/min. Fourier transform infrared (FT-IR) spectra were recorded with a Digilab Excalibur FTS 3000 series FT-IR Spectrometer using KBr pellets. A UV-1800 Shimadzu spectrophotometer was used to monitor the catalytic reaction for kinetic study.

2.5. Catalytic reduction of nitroaromatics

To evaluate catalyst activity, 1.0 mL aqueous solution containing 10.0 mM nitroaromatic (2-NP, 4-NP, 2-NA and 4-NA) was mixed with 29.0 mL freshly prepared 0.045 M NaBH$_4$ solution. Then, Ag/C catalyst was added to the mixture solution with specified ratio of $n_{Ag}:n_{4-NP}:n_{NaBH4} = 1:10:1400$. At a given reaction time, 1.0 mL reaction solution was sampled through a 0.2 μm membrane filter and UV–vis absorption spectrum was recorded within the wavelength range of 250–500 nm. The rate constant of the reduction reaction was calculated by measuring the peak intensity evolution at wavelength of 415, 400, 412 and 380 nm for 2-NP, 4-NP, 2-NA and 4-NA, respectively. To study the reaction kinetics, the reduction reaction was conducted at three different temperatures of 293, 298 and

Scheme 1. Schematic synthetic procedure from cotton to Ag/C nanocomposites.

303 K. Catalyst stability was evaluated by conversion rate for up to 10 cycles.

3. Results and discussion

3.1. Overview of material synthesis

Scheme 1 illustrates the schematic synthetic procedure of carbon support and corresponding Ag/C nanocomposite. Starting from (a) cotton fabric, which is rich in carbon and composed of 95–99% cellulose [30], carbon fabric (b) could be manufactured by applying a thermal treatment process at 800 °C in N_2 atmosphere. With the aim to control nanoparticle size and dispersion, abundant reactive functional groups or sufficient surface defects are preferred on carbon support. In this work, (c) the carbonized cotton (C-cotton) was further treated by a simple oxidation process in air at elevated temperatures. With the presence of oxygen, part of the surface carbon was oxidized into oxygen-containing groups including but not limit to carboxyl, ketone, and hydroxyl [31]. Together with the surface property change, the carbon microstructure evolution (mesopore creation) was also observed by oxidation. (d) Once the surface functionality and mesopore creation was optimized by oxidation step, the carbon was used as reactive support to *in-situ* nucleate/grow metallic Ag nanoparticles with controlled particle size and distribution, Scheme 1.

3.2. Optimizing porous carbon support

In order to optimize the oxidation process, programmed thermal gravitational analysis was performed in air on C-cotton with temperature up to 500 °C, Fig. 1. The sample was firstly heated to 250 °C and kept isothermally for 60 min. The observed weight loss below 200 °C is ascribed to the removal of physically adsorbed water [26]. Then, the temperature was programmed to gradually increase to 500 °C with 60 min isotherm duration after each step increase. As shown in inset of Fig. 1, weight loss rate is negligible before 330 °C and after that goes up exponentially. At 330 °C, the weight loss rate is only 0.25% h^{-1}, which sharply increases to 1.3, 2.1, 3.7, 6.5, 15.2 and 28.1% h^{-1} with increasing temperature to 350, 370, 390, 410, 430 and 450 °C. It is worth mentioning that white ash was observed when the oxidation temperature goes beyond 375 °C indicating the undesirable decomposition of carbon support. Therefore, the oxidation temperature is strictly controlled below 375 °C.

Surface morphology of the carbon support before and after oxidation process was characterized by SEM, Fig. 2(a–d). Obviously, C-cotton and C-250 show relatively smooth surface, Fig. 2(a and b). With increasing temperature to 350 °C, the carbon surface becomes rough and pore structure can be visually observed in Fig. 2(c). Further increasing oxidation temperature to 370 °C creates significant

amount of pores on the surface. EDX was conducted to analyse the elemental species on the surface. The O element fraction in C-cotton and C-250 is about the same as 5.42% and 5.04%, respectively, inset of Fig. 2(a and b). Higher oxidation temperature introduces larger fraction of O element, especially at 370 °C the O fraction of 11.52% is more than doubled than that of C-250, which indicates that the carbon surface has been successfully enriched with oxygen containing functional groups. It is also worth mentioning that the fibrous morphology is well maintained after the carbonization process and even oxidized at 370 °C, Fig. 2(e and f). More importantly, pore structure is not only formed on the surface, but also been created in the internal area of carbon fabric as evidenced by the inset of Fig. 2(e and f). It is concluded that both porous structure and oxygen-containing functional groups have been successfully created through this simple oxidation process.

N_2 adsorption–desorption isotherms were conducted at 77 K to characterize the pore structure and surface area of the oxygenated carbon materials, Fig. 3. The adsorption branch is composed of two characteristic regions: one is at lower relative pressure ($p/p_0 < 0.2$) where the uptake of significant amount of nitrogen occurred; the other is at higher relative pressure ($0.2 < p/p_0 < 0.8$), where the rate of N_2 adsorption slows down and a broad hysteresis loop was observed. Both C-250 and C-350 present type I isotherm curve, indicating the majority of micropores [32]. While C-370 represents typical type IV isotherm with enlarged H$_4$ hysteresis loop, which confirms the presence of mesopores [33]. Embedded table in Fig. 3 summarizes the specific surface area, average pore size and pore volume of the oxygenated carbons. Apparently, the BET surface area and average pore volume increase with increasing oxidation temperature, while the average pore size decreases continuously
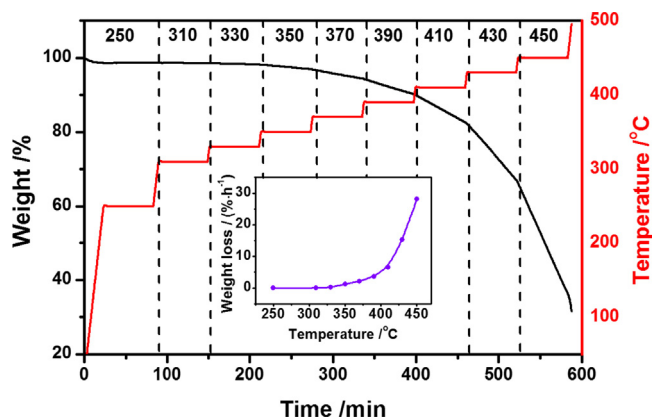

Fig. 1. TGA curve and temperature programing curve of C-cotton. The inset is the weight loss rate curve as a function of temperature. Heating rate: 10 °C min^{-1}.
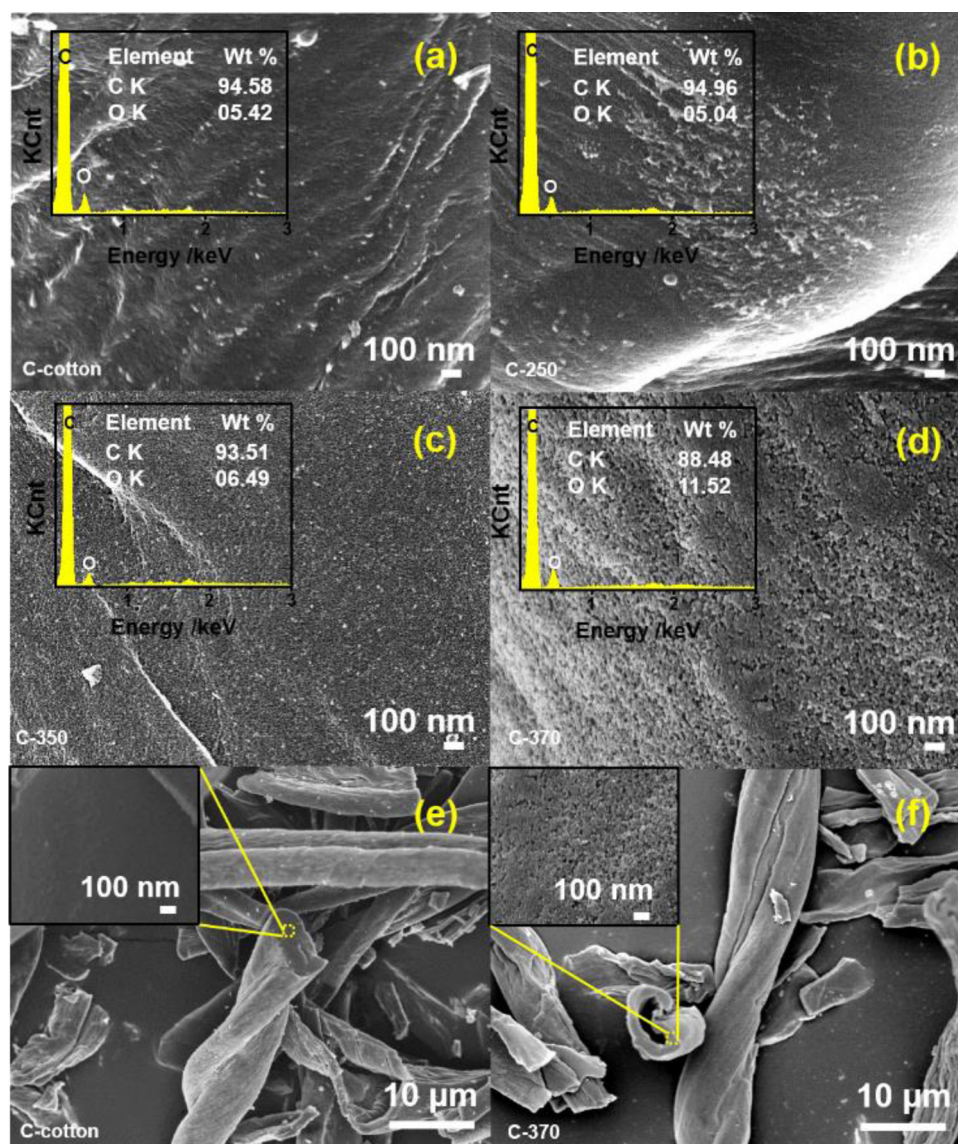
Fig. 2. SEM surface texture of (a) C-cotton, (b) C-250, (c) C-350 and (d) C-370 and their corresponding EDX spectrum (inset figures); cross section area of (e) C-cotton and (f) C-370.

indicating that larger fraction of micropores are generated together with mesopores at 370 °C.

To have a better understanding of the surface property, FT-IR was performed on all the four carbon materials and it is found that hydroxyl, carboxylic and quinone groups were generated by oxidation at 370 °C, Fig. S1. Temperature programmed decomposition profile, Fig. S2, also confirmed the generation of oxygen-containing group on carbon surface after oxidation, which is evidenced by the intensified CO and CO_2 peaks. The CO_2 peak at around 650 °C is associated with the decomposition of carboxylic anhydrides or lactones [31]. The CO profile shows a dominant decomposition beginning at 670 °C with additional contributions at lower temperature of ~230 °C. The CO peak at 670 °C is associated with the decomposition of phenol, quinone, and ether groups [34]. The shoulder at about 280 °C could be attributed to the decomposition of the ketone or aldehyde groups.

To quantify these different groups, XPS characterization was performed on C-cotton and C-370, Fig. 4(a). The main peaks at 531.5 and 282.2 eV are assigned to the O 1s and C 1s [24]. The atomic fraction of oxygen increases by 48% after oxidation at 370 °C, inserted table in Fig. 4(a). This result is consistent with the EDX analysis in Fig. 2. C1s peak deconvolution on C-cotton and C-370 is presented in Fig. 4(b and c) and the corresponding analysis is summarized in Table 1. It is revealed that larger fraction of oxygen-containing functional groups is generated after oxidation including C—O (286.5 eV), C=O (287.2 eV) and O=C—OR/O=C—OH (288.5 eV) [35]. The ratio of C—O—C/C—C bond decreased from 13.6% to 12% after oxidation, which indicates that C—O—C bond cleavage also occurred to form hydroxyl, aldehyde, and carboxyl groups. All these features play significant roles in controlling silver nanoparticle size and dispersion.

Table 1
Results of deconvolution of C1s peaks for C-cotton and C-370.

Sample	Relative area of different chemical bonds (%)				
	C—C	C—O—C	C—O	C=O	COOR
C-cotton	82.21	11.19	4.66	1.94	–
C-370	77.11	9.29	7.34	3.30	2.96

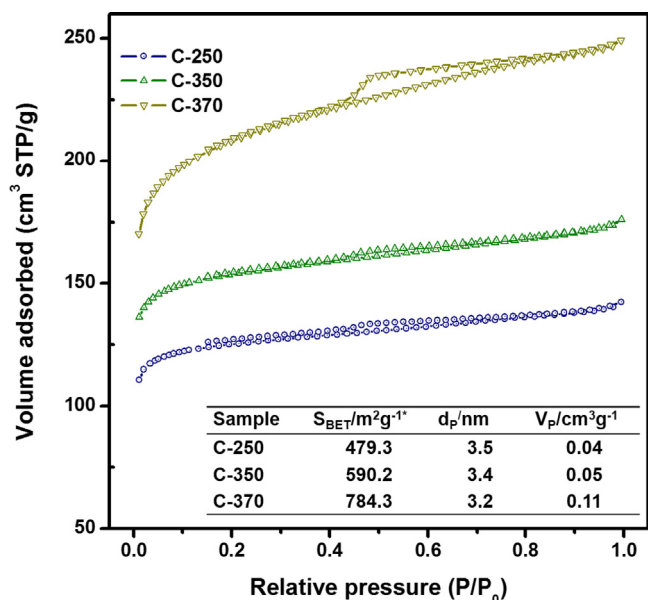| Sample	S_{BET}/m^2g^{-1*}	d_P/nm	V_P/cm^3g^{-1}
C-250	479.3	3.5	0.04
C-350	590.2	3.4	0.05
C-370	784.3	3.2	0.11

Fig. 3. N_2 adsorption–desorption isotherm and structure results of C-250, C-350 and C-370.

3.3. Synthesize Ag/C nanocomposite catalysts

C-cotton and three oxygenated carbons were firstly tested as catalyst supports to grow Ag nanoparticles. Even following the same reaction condition, the uptake of Ag on various carbon supports differs from each other, *e.g.* 2.2, 1.2, 1.5 and 2.2 wt% on C-cotton, C-250, C-350 and C-370, respectively, as revealed by TGA results in Fig. S3. From TEM results in Fig. S5, the typical Ag particle size on C-cotton and C-250 was observed in the range of 100–300 nm with obvious aggregation. The particle size decreases to 10–30 nm on C-350 and surprisingly further decreases to around 3 nm on C-370 without aggregation. The well controlled particle size and distribution is attributed to the large surface area and abundant surface functional groups of C-370. The functional groups provide active sites to react with Ag precursor and localize the particle nucleation/growth. By providing large surface area, particle aggregation could be greatly eliminated and thus the mono-dispersion of Ag nanoparticles was observed.

Once the C-370 is confirmed as the best catalyst support among the four tested carbons, Ag/C-370 nanocomposites with three different Ag loadings of 2.2, 4.4 and 13.6 wt% are synthesized (particle loading is determined by TGA, Fig. S6). FT-IR analysis was performed to understand the surface reaction occurred during nanoparticle formation, Fig. S7. It is observed that the band intensity at $\sim$3400 cm^{-1} (O—H stretching vibration) and 2880–2840 cm^{-1} (C—H vibration) decreases after the reaction, especially both bands nearly disappeared as the Ag loading goes up to 13.6 wt%. These results suggest that —CH$_2$OH groups on carbon surface directly involved in the redox reaction for Ag nanoparticle formation, which is consistent with previous literature reports [24,36].

Confirmed by TEM results in Fig. 5, the Ag nanoparticle size is well controlled below 5.0 nm on C-370 even with high mass loading of 13.6 wt%. The particles are well distributed on carbon support without aggregation. The statistic size distribution of >500 Ag particles is summarized in the inset of Fig. 5(a–c) with mean particle size of 3.03, 3.09 and 4.49 nm, respectively. Fig. 5(d) shows high-resolution TEM image of single Ag nanoparticle taken from Ag-1/C-370. The lattice fringe spacing is measured as 0.23 nm, which corresponds to the (1 1 1) plane of the face-centered-cubic (fcc) Ag crystal.[37] The corresponding fast Fourier transform (FFT) pattern (inset at right corner of Fig. 5d) of the HRTEM image also indicates the high crystallinity of Ag nanoparticles. These results are highly consistent with XRD results, where the diffraction peaks at 38.1° (1 1 1), 44.3° (2 0 0) and 64.4° (2 2 0) can be readily indexed to the face-centered-cubic structure of Ag (JCPDS card no. 4-783), Fig. S8.

3.4. Model reactions for catalyst activity evaluation

Catalytic reduction of nitroaromatics by an excess amount of NaBH$_4$ was chosen as model reactions to evaluate the activity of the Ag/C nanocomposite catalysts. This reaction is well known for its steady feature when exposed to metallic surfaces [38,39]. For 4-NP reduction, although the reaction is a thermodynamically favorable process with E_0 for 4-NP/4-AP = −0.76 V and H_3BO_3/BH_4 = −1.33 V *versus* a normal hydrogen electrode, it is kinetically restricted in the absence of catalysts. The Ag nanoparticles played a key role in the reaction serving as active electron transfer mediators between BH_4^- and nitroaromatic molecules. Fig. 6(b) shows the typical UV–vis absorption spectra before and after reaction. When small
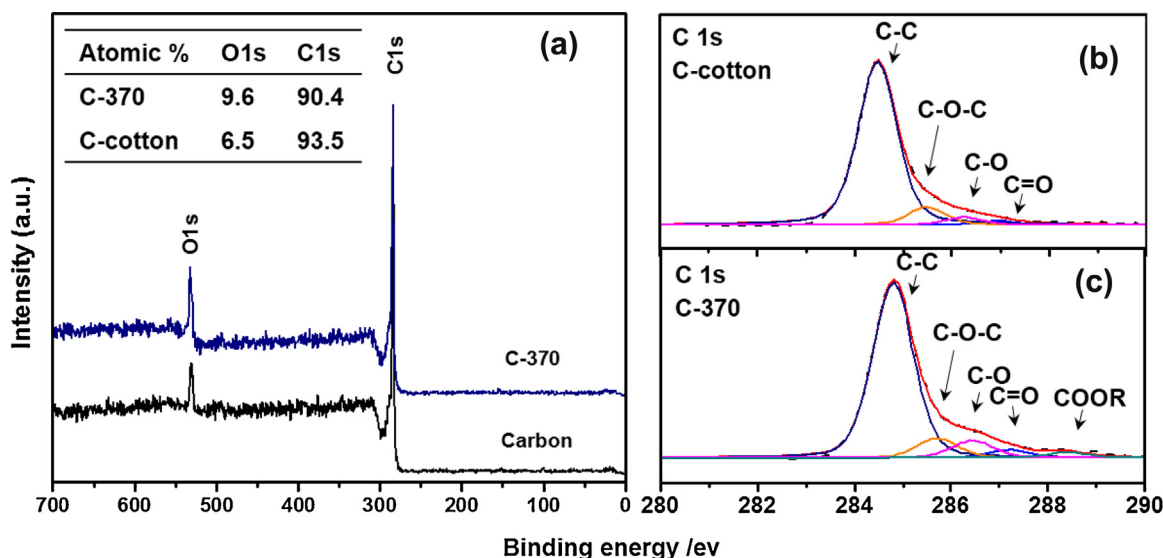

Atomic %	O1s	C1s
C-370	9.6	90.4
C-cotton	6.5	93.5

Fig. 4. (a) XPS full scanned spectra of C-cotton and C-370, (b) C 1s of C-cotton, (c) C 1s of C-370.
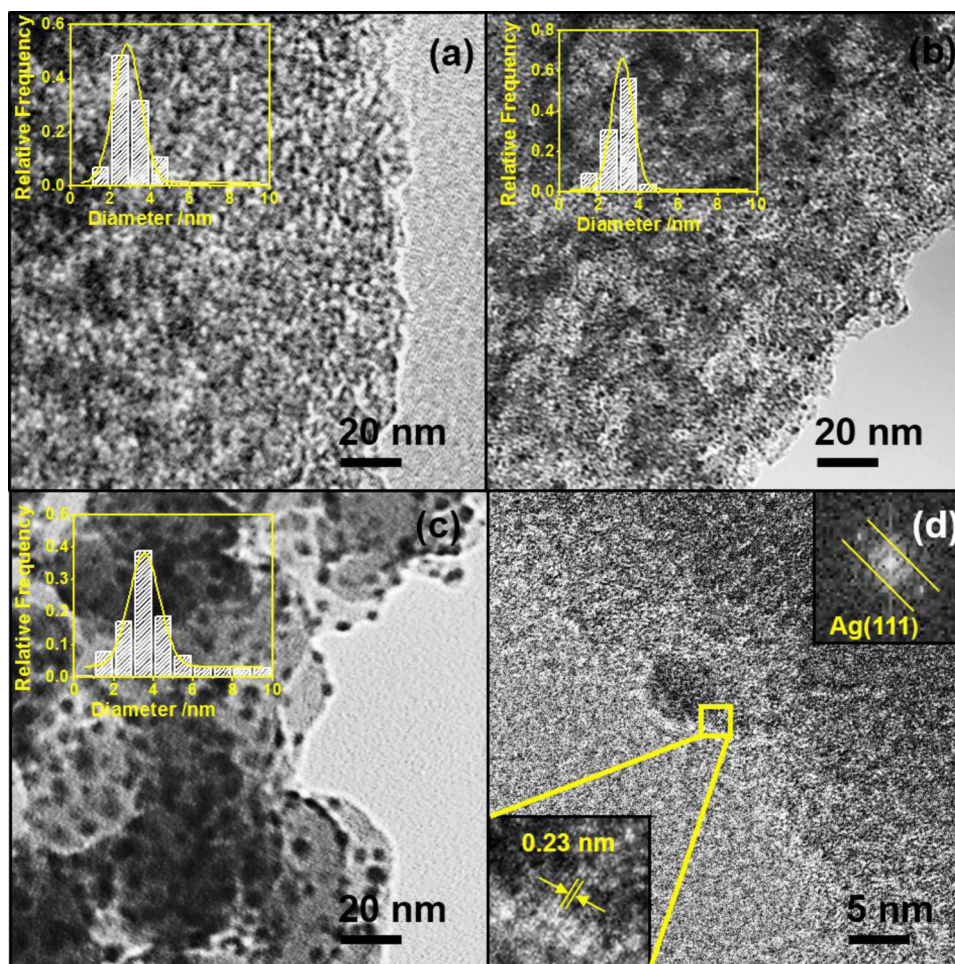
Fig. 5. TEM image of (a) Ag-1/C-370, (b) Ag-2/C-370, (c) Ag-3/C-370 and (d) HRTEM of Ag-1/C-370. The inset figure shows size distribution statistics of each sample.

amount of Ag-1/C-370 catalyst is added into the reaction solution, the broad peak at around 400 nm disappeared completely after one minute. Taken 4-NP as an example, the yellow color of the original reaction solution fades away which corresponds to the gradual decrease of 4-nitrophenolate ions [40]. Meanwhile, a new peak at 300 nm appears that is ascribed to the formation of 4-aminophenol (4-AP) [41]. The disappearance of the peak at 400 nm indicates the completion of the reduction reaction. Reduction reactions of 2-NP, 2-NA and 4-NA are similar to 4-NP reduction and therefore all the flattened adsorption peaks at ~400 nm indicate the fast catalytic reduction reaction between the tested four nitroaromatics and Ag-1/C-370 catalyst, Fig. 6(a, c and d).

Reaction rate is assumed to be independent of NaBH$_4$ concentration since NaBH$_4$ is used in excess amount compared to nitroaromatics. Therefore, the catalytic reactions follow a pseudo-first-order kinetic model [42,43] Taking 4-NP reduction as an example, the C_t/C_0 ratio (C_0: initial 4-NP concentration; C_t: 4-NP concentration at time t) is obtained from the ratio of the absorbance intensity A_t/A_0 (A = absorbance at 400 nm), and the rate constant k can be calculated by Eq. (1):

$$\frac{d\left(\ln\left(A_t/A_0\right)\right)}{dt} = \frac{d\left(\ln\left(C_t/C_0\right)\right)}{dt} = -k \tag{1}$$

3.5. Effect of oxidation temperature

To screen the catalyst activity, 4-NP reduction reaction was performed over the Ag/C catalysts, Fig. 7. The highly linear relation of ln(C_t/C_0) *versus* time indicates the reduction reaction follows the

pseudo-first-order kinetics. The rate constant k was assessed to be 4.4×10^{-4}, 1.5×10^{-2}, 4.13×10^{-2} and $0.17\,\text{s}^{-1}$ for Ag/C-cotton, Ag/C-250, Ag/C-350 and Ag/C-370, respectively. Ag/C-370 exhibited the highest catalytic activity among the four samples, which could be attributed to the smallest Ag nanoparticle size and highest dispersion quality achieved. The poor performance of Ag/C-cotton and Ag/C-250 are associated with the large and irregular shape of Ag nanoparticles, Fig. S5. XPS deconvolution analysis of Ag 3d peaks further reveals the major component of Ag^0 (368.2 eV for Ag^0 3d$_{5/2}$, 374.2 eV for Ag^0 3d$_{3/2}$) and minor component of Ag—O— in Ag/C-cotton, while only pure Ag^0 is obtained in Ag/C-370, Fig. 8. The existence of inactive Ag compound is due to the incomplete reduction on less reactive surfaces, which results in the low catalytic activity of Ag/C-cotton.

3.6. Effect of Ag nanoparticle loading

Before evaluating the activity of Ag/C-370 catalysts, a control test on pure C-370 was conducted. The flat curve indicates that C-370 is not reactive with 4-NP and also the 4-NP adsorption on C-370 can be neglected, Fig. 9. Using the slope of linear fitting curves, the rate constant k can be calculated as 0.08, 0.12 and 0.10 s^{-1} for Ag-1/C-370, Ag-2/C-370 and Ag-3/C-370, respectively. Ag-2/C-370 exhibits the highest catalytic activity among the samples. Even though Ag-3/C-370 has larger Ag loading, the relatively larger particle size exposes less surface atoms and thus lower activity was observed compared to Ag-2/C-370. To compare the catalytic activity with previously reported catalysts employed for
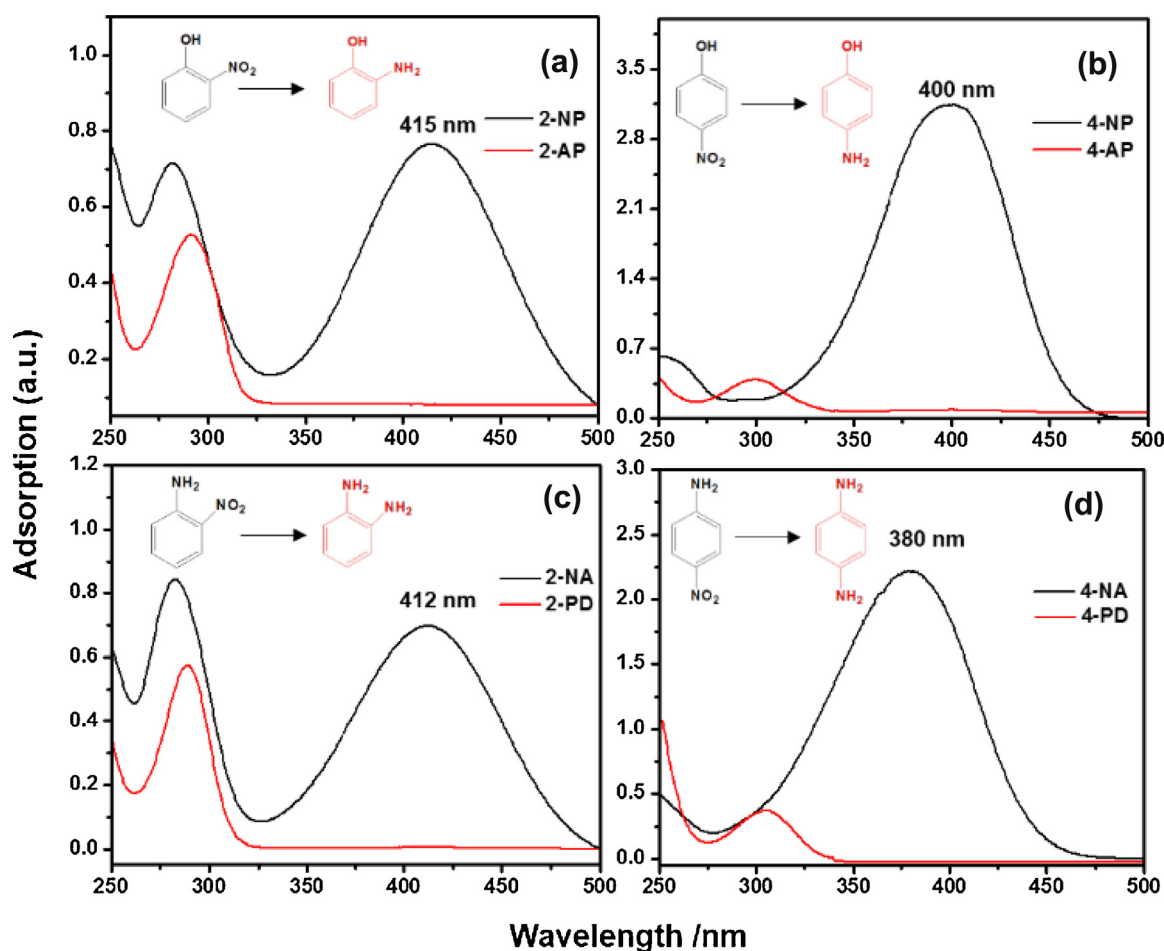
Fig. 6. The UV–vis spectra of nitroaromatics reduction into amino-aromatics in aqueous solution. (a) 2-NP to 2-aminophenol (2-AP), (b) 4-NP to 4-aminophenol (4-AP), (c) 2-NA to 2-phenylenediamine (2-PD) and (d) 4-NA to 2-phenylenediamine (4-PD). [nitroaromatics] = 0.3 mM, [NaBH$_4$] = 40 mM, [Ag-1/C-370] = 3 mg/L, reaction time: 1 min.

4-NP reduction, k' ($k' = k/m$) is introduced which normalizes the rate constant k by the total mass (m) of the catalyst [44]. As shown in Table 2, k' of the Ag/C-370 catalysts is significantly larger than all the listed Ag/carbon (Ag/C spheres, Ag/Mesoporous C and Ag/CNFs) and Ag/oxide (Ag/Fe$_3$O$_4$@C, Ag/FeO$_X$, Ag/SiO$_2$ and Ag/CPSA@MATP) catalysts as well as other metal (Au/TiO$_2$, Pd/C spheres, Ni/SNTs and Au/Fe$_3$O$_4$) catalysts from literature reports.

The superior catalytic activity of Ag/C-370 in this work is mainly attributed to following two factors. First of all, small particle size with controlled mono-dispersion. Ag nanoparticles with diameter of less than 5 nm expose significantly larger amount of surface active sites for efficient reaction compared with particles larger than 10 nm. It is well known that oxygen atom exists in each pyranose ring of the cellulose molecule. Upon oxidation, it is assumed that the oxygen-containing groups can be generated evenly at

Table 2
Comparison of catalyst activity with literature reports in 4-NP reduction.

Catalyst	[4-NP] (mM)	k (s^{-1}) × 10^2	k/m (k′, s^{-1} g^{-1})	TOF (s^{-1}) × 10^{-2}	Particle size (nm)	References
Ag-1/C-370	0.3	8	26.7	27	3.0	This work
Ag-2/C-370	0.3	12	40.0	20	3.1	This work
Ag-3/C-370	0.3	10	33.3	7	3.5	This work
Ag/C spheres	0.05	0.17	1.69	0.01	10	[45]
Ag/Mesoporous C	0.12	0.53	2.66	0.6	13.2	[46]
Ag/CNFs[a]	0.12	0.62	6.2	1.0	25.7	[47]
Ag/Fe$_3$O$_4$@C	0.2	1.72	0.86	–	–	[48]
Ag/FeO$_X$	0.02	0.30	3.00	0.2	11.3	[49]
Ag/SiO$_2$	0.12	0.12	0.25	0.2	~35	[50]
Ag/CPSA@MATP[b]	3.3	1.43	0.287	1.1	~25	[51]
Au/TiO$_2$	3	0.71	0.12	1.3	7.1	[52]
Pd/C spheres	0.05	0.23	2.3	0.01	8.8	[53]
Ni/SNTs[c]	0.25	8.4	21	0.1	~50	[54]
Au/Fe$_3$O$_4$	0.2	1.05	5.25	–	11.2	[55]

[a] CNFs-carbon nanofibers.

[b] CPSA@MATP-magnetic attapulgite nanocomposite grafted crosslinked copolymer.
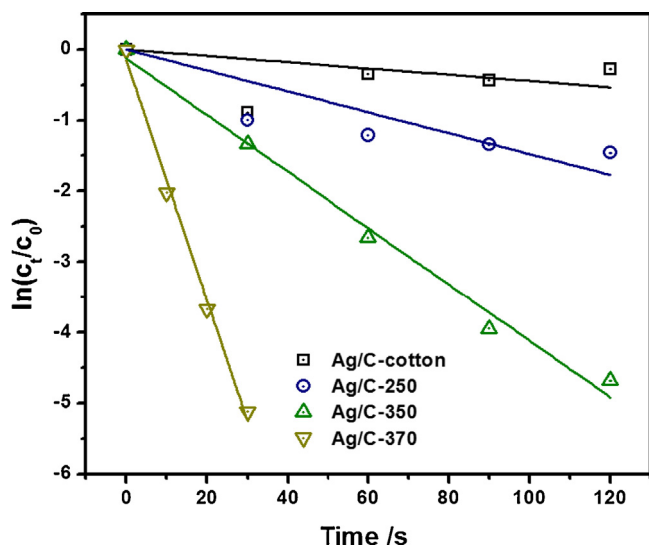
[c] SNTs-silica nanotubes.

Fig. 7. Plots of $\ln[C_t/C_0]$ *versus* reaction time for 4-NP reduction over Ag/C catalysts. [4-NP] = 0.3 mM, [NaBH$_4$]/[4-NP] = 80, [catalyst] = 0.16 mg/mL.

Fig. 9. Plots of $\ln[C_t/C_0]$ *versus* reaction time for the reduction of 4-NP with NaBH4 over different loading Ag/C nanocatalysts. [4-NP] = 0.3 mM, [NaBH$_4$]/[4-NP] = 80, [catalyst] = 0.16 mg/mL.

molecular level and distributed uniformly throughout the surface, which definitely benefits the size and dispersion control of metal nanoparticles. Secondly, meso/micro hierarchical pore structure and hydrophilic surface character facilitate mass transfer of reactant/product over catalyst surface. Fig. S9 gives the water contact angle results on Ag/C-cotton and Ag/C-370 by static contact angle mode. Water contact angle is significantly reduced from 139.7 to 47.3° after oxidation, indicating a much more hydrophilic surface of Ag/C-370 compare with Ag/C-cotton. The hydrophilic surface character enables the faster diffusion of aqueous reactants into inner active sites of catalyst and allows maximum possible catalyst participating in the reactions.

Another important parameter that reflects catalyst efficiency is called turn-over frequency (TOF). The TOF is defined as moles (or numbers) of the product molecules generated per moles (or numbers) of catalyst surface atoms [56]. Most of the existing work use moles of active component instead the moles of surface atoms due to the challenge in precise quantify of surface atoms [49,54,57]. The TOF of Ag-1/C-370, Ag-2/C-370 and Ag-3/C-370 for 4-NP reduction reaction was calculated as 0.27, 0.20 and 0.07 s^{-1}. The activity of Ag nanoparticles in Ag-1/C-370 and Ag-2/C-370 is obviously higher than Ag in Ag-3/C-370. The lower TOF value of Ag-3/C-370 is due to its relatively larger particle size (Fig. 5), where larger portion
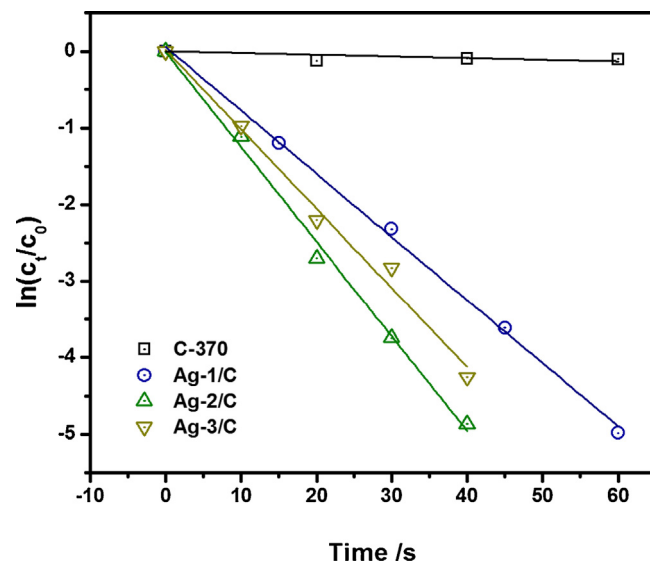
of Ag atoms are embedded inside particle rather than on surface participating reactions.

3.7. Nitroaromatics reduction reaction kinetics

Activation energy (E_a) is an empirical parameter that represents the energy required to overcome the energy barrier for specific chemical reactions [58,59]. To acquire E_a for different reactions, the catalytic reaction was performed at three temperatures of 293, 298 and 303 K. The reduction reactions with 4 different nitroaromatics (2-NP, 4-NP, 2-NA and 4-NA) and Ag-1/C-370 catalyst are shown in Fig. 10. The reaction rates all increase with increasing reaction temperature from 293 to 303 K. The E_a can be assessed from the Arrhenius Eq. (2):

$$k = A \times \exp\left(\frac{-E_a}{RT}\right) \tag{2}$$

where A is Arrhenius factor, k is the rate constant of the reaction at temperature T. E_a can be calculated from the slope of *lnk versus* $1/T$ linear curve (the inset of Fig. 10). The E_a value is 86.73, 36.28, 52.94 and 43.05 kJ/mol for 2-NP, 4-NP, 2-NA and 4-NA, respectively. Experienced from previous studies, activation energy differs appreciably
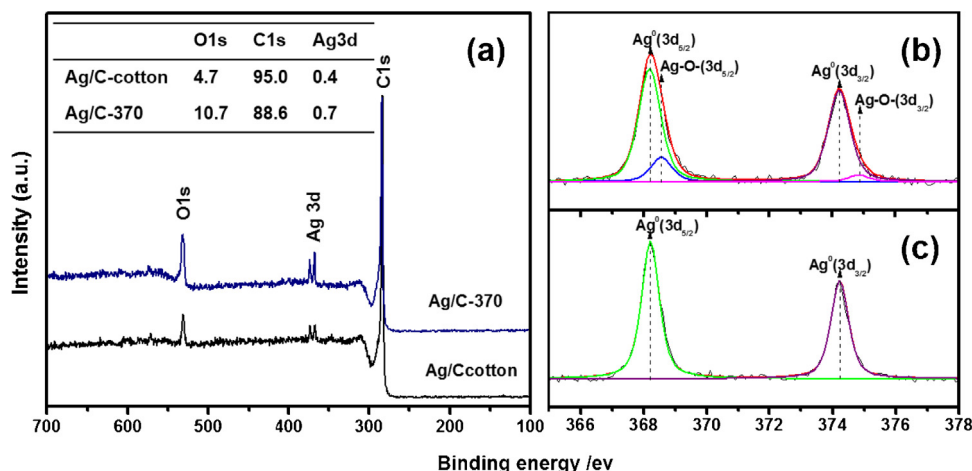

Fig. 8. (a) XPS full scanned spectra of Ag/C-cotton and Ag/C-370, (b) Ag 3d of Ag/C-cotton, (c) Ag 3d of Ag/C-370.
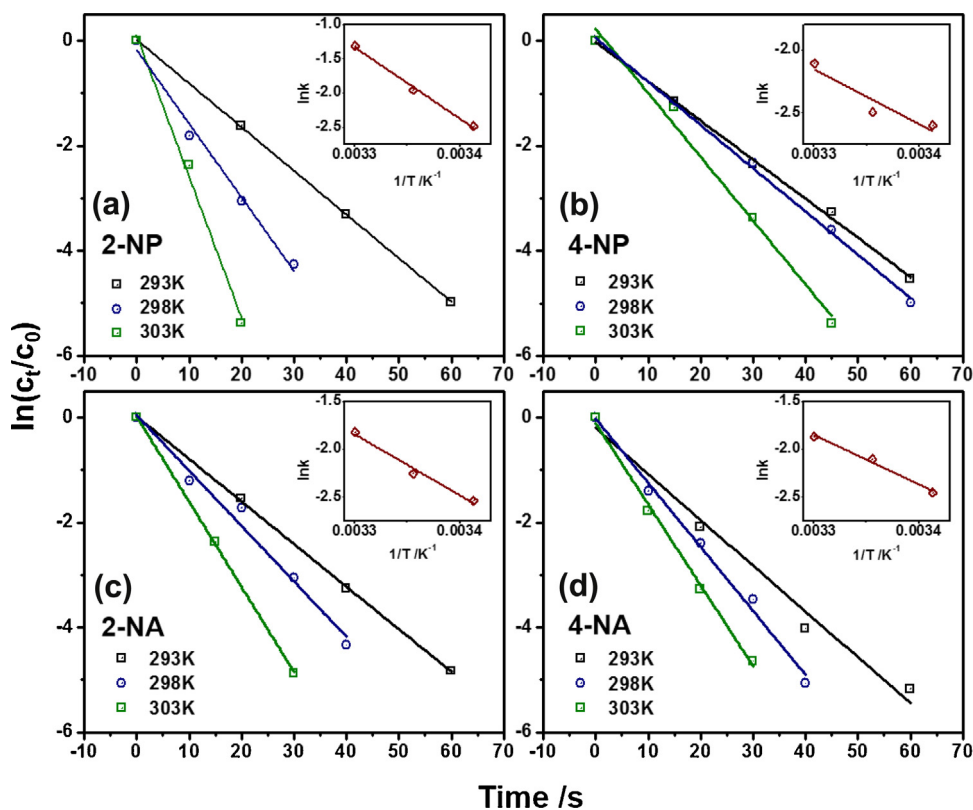
Fig. 10. Plots of $\ln[C_t/C_0]$ *versus* reaction time for the reduction of nitroaromatics, (a) 2-NP, (b) 4-NP, (c) 2-NA and (d) 4-NA, over Ag-1/C-370 at different temperatures. [NP or NA] = 0.3 mM, [NaBH$_4$]/[NP or NA] = 80, [catalyst] = 0.10 mg/mL. The inset indicates the corresponding Arrhenius plot.

for different reactions. The difference of E_a value could ascribe to the diffusional barriers in the system [60,61]. For surface catalyzed reactions, the activation energy lies within 5–50 kJ/mol. Hence, the reactions of 4-NP, 2-NA and 4-NA are more likely a diffusion controlled process on the surface of Ag/C catalysts, while reaction of 2-NP is suggested as a reaction-controlled process.

3.8. Catalyst durability evaluation

Catalyst durability is critically important in practical applications. In this work, the Ag-1/C-370 catalyst was tested in the

Fig. 11. Conversion rate of 2-NP, 4-NP, 2-NA and 4-NA with cycling test.

reduction reactions with 4 different nitroaromatics for up to ten cycles. After each test, the catalyst was separated from the reaction mixture rapidly and rinsed with deionized water, and then reused in the next cycle. As shown in Fig. 11, the conversion rate for all the four nitroaromatics remains >98% after 10 cycles, indicating the well remained catalyst activity after cycling tests.

4. Conclusions

To be concluded, consecutive carbonization and thermal oxidation processes are used to successfully process cotton fabric into mesoporous carbon support. The whole process does not involve any chemicals. By optimizing the oxidation profile, porous carbon with large surface area of 784.3 m^2/g and mesopore structure can be fabricated. These porous carbons also feature abundant oxygen-containing surface functional groups, which are ready to react with Ag precursor and form metallic nanoparticles. Both surface area and surface groups are essential to control Ag nanoparticle size and dispersion. On the oxygenated carbon substrate processed at 370 °C, Ag nanoparticle size can be well controlled below 5 nm even the mass loading is as high as 13.6 wt%. These catalysts show very fast reaction rate in nitroaromatics (2-NP, 4-NP, 2-NA and 4-NA) reduction, which could attribute to the highly reactive <5 nm Ag nanoparticles and open mesoporous structure of carbon substrate that facilitates the efficient transport of reactant/product over catalyst surface. The green feature of process cotton into advanced catalyst support opens versatile possibilities in broader scope of biomass utilization and metal/carbon hybrid catalyst development for emerging energy and environmental areas.

Appendix A. Supplementary data

Supplementary data associated with this article can be found, in the online version, at http://dx.doi.org/10.1016/j.apcatb.2015.09.024.

References

[1] C. Zhang, S.Y. Hwang, A. Trout, Z. Peng, J. Am. Chem. Soc. 136 (2014) 7805–7808.
[2] K.H. Lim, H. Kim, Appl. Catal. B 158 (2014) 355–360.
[3] K.P. De Jong, J.W. Geus, Catal. Rev. 42 (2000) 481–510.
[4] L. Chen, J. Zhu, Chem. Commun. 50 (2014) 8253–8256.
[5] J. Zhu, M. Chen, H. Qu, Z. Luo, S. Wu, H.A. Colorado, S. Wei, Z. Guo, Energy Environ. Sci. 6 (2013) 194–204.
[6] S. Radhakrishnan, K. Krishnamoorthy, C. Sekar, J. Wilson, S.J. Kim, Appl. Catal. B 148 (2014) 22–28.
[7] T.-W. Lin, C.-J. Liu, C.-S. Dai, Appl. Catal. B 154 (2014) 213–220.
[8] J. Zhu, S. Wei, H. Gu, S.B. Rapole, Q. Wang, Z. Luo, N. Haldolaarachchige, D.P. Young, Z. Guo, Environ. Sci. Technol. 46 (2012) 977–985.
[9] R. Pereira, M. Pereira, M. Alves, L. Pereira, Appl. Catal. B 144 (2014) 713–720.
[10] Z. Huang, F. Li, B. Chen, F. Xue, Y. Yuan, G. Chen, G. Yuan, Green Chem. 13 (2011) 3414–3422.
[11] J. Pang, A. Wang, M. Zheng, Y. Zhang, Y. Huang, X. Chen, T. Zhang, Green Chem. 14 (2012) 614–617.
[12] S.-J. Park, Y.-S. Jang, J. Colloid Interface Sci. 261 (2003) 238–243.
[13] M. Ghaedi, Spectrochim. Acta Part A 94 (2012) 346–351.
[14] Y. Wang, Y. Wan, X. Dong, G. Cheng, H. Tao, T. Wen, Carbon 36 (1998) 1567–1571.
[15] S.H. Joo, S.J. Choi, I. Oh, J. Kwak, Z. Liu, O. Terasaki, R. Ryoo, Nature 412 (2001) 169–172.
[16] S. Ikeda, S. Ishino, T. Harada, N. Okamoto, T. Sakata, H. Mori, S. Kuwabata, T. Torimoto, M. Matsumura, Angew. Chem. 118 (2006) 7221–7224.
[17] Z. Xue, F. Zhang, D. Qin, Y. Wang, J. Zhang, J. Liu, Y. Feng, X. Lu, Carbon 69 (2014) 481–489.
[18] A.A. Nair, R. Sundara, N. Anitha, Int. J. Hydrogen Energy 40 (2015) 3259–3267.
[19] Y. Chi, L. Zhao, Q. Yuan, X. Yan, Y.J. Li, N. Li, X.T. Li, J. Mater. Chem. 22 (2012) 13571–13577.
[20] L.-Z. Fan, S. Qiao, W. Song, M. Wu, X. He, X. Qu, Electrochim. Acta 105 (2013) 299–304.
[21] M.-M. Titirici, M. Antonietti, Chem. Soc. Rev. 39 (2010) 103–116.
[22] Y. Wang, Z.M. Liu, B.X. Han, Y. Huang, G.Y. Yang, Langmuir 21 (2005) 10846–10849.
[23] P.W. Albers, J. Pietsch, J. Krauter, S.F. Parker, PCCP 5 (2003) 1941–1949.
[24] T. Ji, L. Chen, M. Schmitz, F.S. Bao, J. Zhu, Green Chem. 17 (2015) 2515–2523.
[25] F. Xie, J.J. Hu, C.C. Jin, Q. Wang, J. Exp. Nanosci. 8 (2013) 661–668.
[26] T. Ji, L. Li, M. Wang, Z. Yang, X. Lu, RSC Adv. 4 (2014) 29591–29594.
[27] Z. Wu, Y. Mao, X. Wang, M. Zhang, Green Chem. 13 (2011) 1311–1316.
[28] Z. Guo, Y. Chen, L. Li, X. Wang, G.L. Haller, Y. Yang, J. Catal. 276 (2010) 314–326.
[29] Z. Shen, Y. Luo, Q. Wang, X. Wang, R. Sun, ACS Appl. Mater. Interfaces 6 (2014) 16147–16155.
[30] H. Kim, J. Ralph, RSC Adv. 4 (2014) 7549–7560.
[31] J. Figueiredo, M. Pereira, M. Freitas, J. Orfao, Carbon 37 (1999) 1379–1389.
[32] Y. Zhao, Z.Q. Wang, X. Zhao, W. Li, S.X. Liu, Appl. Surf. Sci. 266 (2013) 67–72.
[33] N.R. Khalili, M. Campbell, G. Sandi, J. Golaś, Carbon 38 (2000) 1905–1915.
[34] S. Kundu, Y. Wang, W. Xia, M. Muhler, J. Phys. Chem. C 112 (2008) 16869–16878.
[35] S. Peng, Z. Gao, J. Sun, L. Yao, Y. Qiu, Appl. Surf. Sci. 255 (2009) 9458–9462.
[36] Z.-W. He, Q.-F. Lu, J.-Y. Zhang, ACS Appl. Mater. Interfaces 4 (2012) 369–374.
[37] W. Ye, X. Shi, J. Su, Y. Chen, J. Fu, X. Zhao, F. Zhou, C. Wang, D. Xue, Appl. Catal. B 160 (2014) 400–407.
[38] D.M. Dotzauer, J. Dai, L. Sun, M.L. Bruening, Nano Lett. 6 (2006) 2268–2272.
[39] J. Zhang, G. Chen, M. Chaker, F. Rosei, D. Ma, Appl. Catal. B 132 (2013) 107–115.
[40] K. Kuroda, T. Ishida, M. Haruta, J. Mol. Catal. A: Chem. 298 (2009) 7–11.
[41] V. Evangelista, B. Acosta, S. Miridonov, E. Smolentseva, S. Fuentes, A. Simakov, Appl. Catal. B 166 (2015) 518–528.
[42] Y. Deng, Y. Cai, Z. Sun, J. Liu, C. Liu, J. Wei, W. Li, C. Liu, Y. Wang, D. Zhao, J. Am. Chem. Soc. 132 (2010) 8466–8473.
[43] S. Gazi, R. Ananthakrishnan, Appl. Catal. B 105 (2011) 317–325.
[44] B. Baruah, G.J. Gabriel, M.J. Akbashev, M.E. Booher, Langmuir 29 (2013) 4225–4234.
[45] S.C. Tang, S. Vongehr, X.K. Meng, J. Mater. Chem. 20 (2010) 5436–5445.
[46] Y. Chi, J.C. Tu, M.G. Wang, X.T. Li, Z.K. Zhao, J. Colloid Interface Sci. 423 (2014) 54–59.
[47] P. Zhang, C.L. Shao, Z.Y. Zhang, M.Y. Zhang, J.B. Mu, Z.C. Guo, Y.C. Liu, Nanoscale 3 (2011) 3357–3363.
[48] M.Y. Zhu, C.J. Wang, D.H. Meng, G.W. Diao, J. Mater. Chem. A 1 (2013) 2118–2125.
[49] J.R. Chiou, B.H. Lai, K.C. Hsu, D.H. Chen, J. Hazard. Mater. 248 (2013) 394–400.
[50] M. Wang, D. Tian, P.P. Tian, L.J. Yuan, Appl. Surf. Sci. 283 (2013) 389–395.
[51] B. Mu, Q. Wang, A.Q. Wang, J. Mater. Chem. A 1 (2013) 7083–7090.
[52] A.A. Ismail, A. Hakki, D.W. Bahnemann, J. Mol. Catal. A: Chem. 358 (2012) 145–151.
[53] S.C. Tang, S. Vongehr, G.R. He, L. Chen, X.K. Meng, J. Colloid Interface Sci. 375 (2012) 125–133.
[54] S. Zhang, S. Gai, F. He, S. Ding, L. Li, P. Yang, Nanoscale 6 (2014) 11181–11188.
[55] F.H. Lin, R.A. Doong, J. Phys. Chem. C 115 (2011) 6591–6598.
[56] J. Lee, J.C. Park, H. Song, Adv. Mater. 20 (2008) 1523–1528.
[57] H. Ozay, Sci. Adv. Mater. 5 (2013) 575–582.
[58] B. Girisuta, L. Janssen, H. Heeres, Green Chem. 8 (2006) 701–709.
[59] M. Liang, R.X. Su, W. Qi, Y.J. Yu, L.B. Wang, J. Mater. Sci. 49 (2014) 1639–1647.
[60] Y. Lu, Y. Mei, R. Walker, M. Ballauff, M. Drechsler, Polymer 47 (2006) 4985–4995.
[61] J. Zeng, Q. Zhang, J. Chen, Y. Xia, Nano Lett. 10 (2009) 30–35.